Thermo-fluid simulation of latent heat thermal energy storage devices using the Particle Finite Element Method

Maxence Claeskens[1], Dorian Bogucki[1], Simon Février[1], Martin Lacroix[1], Romain Boman[1], Jean-Philippe Ponthot[1], and Eduardo Fernández*[1]

[1]Aerospace and Mechanical Engineering, University of Liege, Liege, Belgium
* efsanchez@uliege.be (corr. author)

February 20, 2026

Abstract

Purpose - The aim of this work is to improve the numerical simulation of Thermal Energy Storage systems based on Phase Change Materials (TES–PCM). These systems involve strong nonlinearities due to phase change and natural convection, which makes their design challenging. This study focuses on enhancing computational efficiency and accuracy in modeling the phase transition process through an adaptive mesh strategy within the Particle Finite Element Method (PFEM).

Design/Methodology/Approach - We implement PFEM for the simulation of TES–PCM, allowing dynamic remeshing during computation. A new mesh adaptation strategy is proposed to optimize spatial discretization in the mushy zone, based on thermal gradients rather than distance fields. The methodology is validated using experimental data from the literature and verified through a fin-placement optimization problem.

Findings - The proposed method accurately reproduces experimental melting fronts for lauric acid and gallium while reducing computational time by up to 25% compared to classical mesh adaptation. The approach captures the influence of natural convection and fin placement, confirming its robustness and predictive capability for TES–PCM applications.

Originality/Value - To the best of our knowledge, this is the first application of PFEM to TES–PCM problems. The new mesh adaptation criterion enhances efficiency without compromising accuracy, offering a promising alternative to classical fixed-mesh CFD methods. The findings highlight the potential of PFEM as a flexible and efficient tool for simulating phase change problems and guiding the design of thermal energy storage devices.

Keywords: PFEM; Thermal Energy Storage; Phase Change Material; Adaptive Mesh Refinement

1 Introduction

Current environmental concerns have forced human beings to look for less polluting and ecofriendly technological alternatives. The challenge is placed on all industrial sectors, such as transport, housing, energy, and food, among others (Bouckaert et al., 2021). Some of the pillars of action towards a healthier planet include increasing energy efficiency and the use of renewable energies. An approach that can greatly assist these measures is the use of Thermal Energy Storage (TES) devices (Cabeza, 2021). The idea of TES is to store thermal energy when it is abundant (charging stage), keep it for a period of time (retention stage), and recover it when it is needed (discharge stage).

A TES system can operate on different principles, but one of the most promising methods is using Phase Change Materials (PCMs). The idea is to exploit the latent heat of a material to store or release thermal energy through the melting or solidification process. Thus, it is convenient to use materials with high latent heat of fusion, such as wax, salts or acids (see Zhang et al., 2023, for a more comprehensive list). However, common PCMs present low thermal conductivity, so a second Highly thermally Conductive Material (HCM) must be incorporated into the TES in order to accelerate heat transfer with the external source, as shown in Fig. 1a. Otherwise, the charging

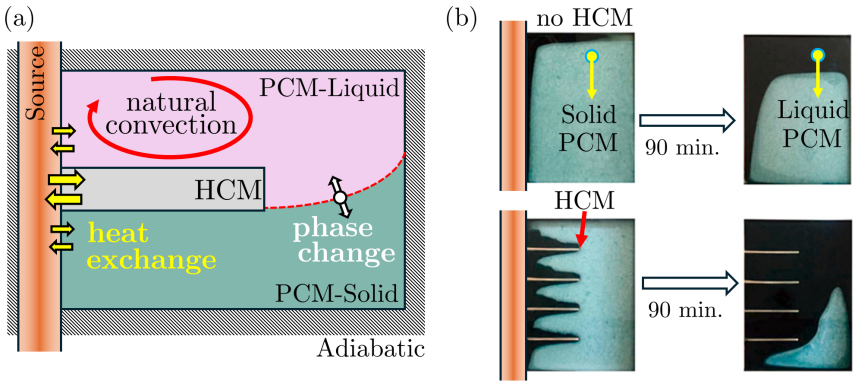

Figure 1: (a) Illustration of the operating principle of a Thermal Energy Storage (TES) device based on Phase Change Material (PCM). (b) Effect of adding a High thermal Conductivity Material (HCM) to accelerate heat transfer between the source and the TES device. The image in (b) is adapted from Joshi and Rathod (2020).

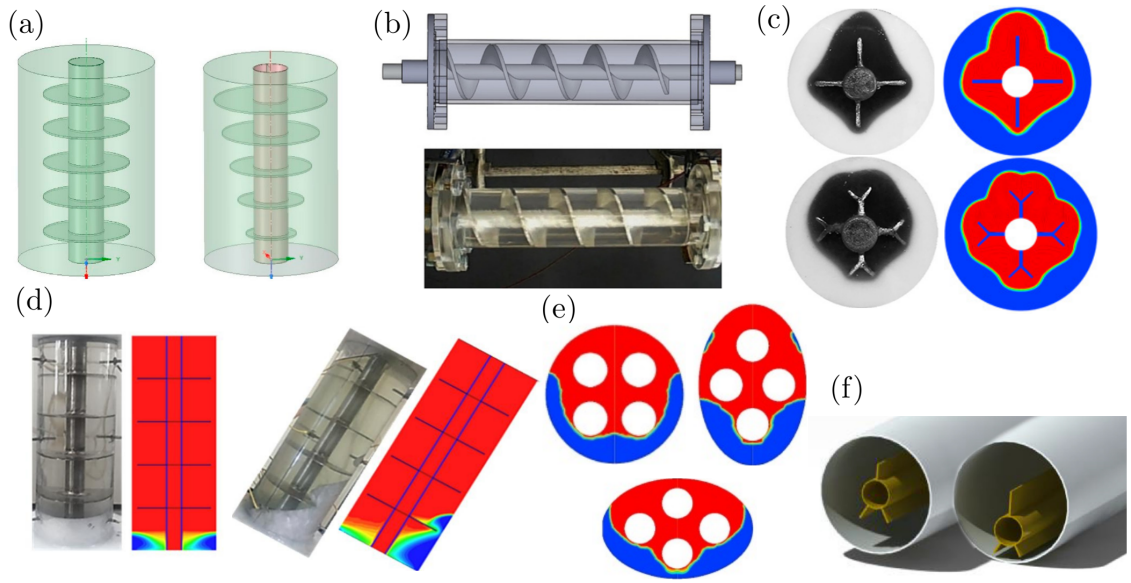

Figure 2: A small collection of design that have been proposed and studied in the TES-PCM literature. (a) Variable fin size (Singh et al., 2019), (b) helical shape (Rozenfeld et al., 2017), (c) Y-branched type (Safari et al., 2021) (d) inclination (Kalapala and Devanuri, 2021), (e) elliptical casing (Pourakabar and Darzi, 2019), and (f) source pipe positioning (Kumar and Verma, 2020).

and discharge stages would take excessive time, as shown in Fig. 1b, reducing the efficiency of the process or even making the TES unfeasible depending on the desired application.

The literature is rich regarding the geometrical design of TES-PCM, showing that performance of TES devices is highly dependent on the arrangement of PCM and HCM. For example, Singh et al. (2019) investigated the use of straight fins (Fig. 2a), Rozenfeld et al. (2017) analysed helical fins (Fig. 2b), and Safari et al. (2021); Liu et al. (2020) examined Y-branched fins (Fig. 2c). Other studies explored additional geometric factors: Pourakabar and Darzi (2019) evaluated the influence of the casing geometry (Fig. 2e), Kalapala and Devanuri (2021); Zhang et al. (2024) investigated the effect of orientation with respect to gravity (Fig. 2d), and Kumar and Verma (2020) focused on the configuration of heat exchange tubes (Fig. 2f). This non-exhaustive review highlights that achieving an optimal TES–PCM design is challenging, as the system is governed by complex coupled phenomena such as phase-change, heat transfer, and natural convection in the liquid PCM. Furthermore, key factors like the choice of PCM, operating temperature range, and cycle duration of the thermal battery significantly influence the optimal design. These examples are presented to illustrate the strong sensitivity of TES–PCM performance to geometric, material, and operating parameters, thereby motivating the need for advanced numerical modeling approaches.

The simulation of TES cycles has been extensively studied in the literature for different types of TES systems, including those based on PCMs. Several modeling approaches have been proposed and validated, among which the enthalpy-porosity method stands out as a high-fidelity model.

In this approach, the energy conservation and Navier-Stokes equations are solved, typically using the Finite Volume Method (FVM) or the Finite Element Method (FEM), while accounting for natural convection and incorporating the Carman-Kozeny term (Carman, 1997; Kozeny, 1927) to model the solid-phase behavior within the fluid equations. The enthalpy-porosity method has been widely validated in the literature for both charging and discharging stages, often using commercial software such as Ansys (Kalapala and Devanuri, 2021; Singh et al., 2019; Kiros et al., 2025; Meng et al., 2025; Agrawal et al., 2025; Nandi and Biswas, 2025; Liu et al., 2024), SpaceClaim (Kang et al., 2025) and Comsol (Akhmetov et al., 2019; Ismail et al., 2024). Due to its high fidelity in capturing the key physical phenomena that govern TES-PCM performance, the enthalpy-porosity method has also been used for geometrical optimization, such as for straight fin sizing (Kiros et al., 2025), optimal fin positioning (Liu et al., 2024), and optimal PCM selection (Kang et al., 2025), among others. This non-exhaustive review reflects a dominant trend in the literature: the use of traditional mesh-based methods like FEM or FVM, typically relying on an Eulerian framework with fixed meshes defined a priori, and the use of commercial software.

The low thermal diffusivity of PCMs, especially when compared to metals, leads to large thermal gradients, particularly in the phase-change (mushy) zone. This necessitates very fine spatial discretizations (meshes) to ensure solution accuracy or convergence (Garoosi et al., 2025). In fixed-mesh methods, this translates into highly refined meshes from the beginning of the simulation, which increases computational cost and limits the scalability of classical methodologies. Beyond fixed-mesh approaches, several adaptive numerical strategies have been proposed to improve the efficiency of phase-change simulations involving natural convection. These include Adaptive Mesh Refinement (AMR) techniques within Eulerian FEM or FVM frameworks, as well as moving-mesh and mesh-redistribution methods, which aim to concentrate resolution in regions of strong thermal or velocity gradients. Such approaches have been successfully applied to solidification and melting problems, particularly to better resolve the mushy zone while limiting computational cost (Sadaka et al., 2020). However, their implementation often relies on complex error estimators, refinement and coarsening procedures, and data-transfer operations between successive meshes. Moreover, applications of AMR within Eulerian FEM or FVM frameworks remain relatively scarce in the specific context of TES–PCM systems, with most studies focusing on benchmark solidification problems or high-diffusivity materials such as gallium rather than on full TES–PCM configurations.

In contrast to the current state of the art, we adopt a relatively recent and simple discretization technique known as the Particle Finite Element Method (PFEM) for the simulation of TES-PCM devices. Originally proposed by Idelsohn et al. (2004), PFEM is a Lagrangian particle-based method that naturally allows for adaptive mesh refinement by simply increasing particle density in regions where finer spatial resolution is required (see Cremonesi et al., 2020, for a comprehensive review). This inherent capability of PFEM is precisely what we seek to exploit in the context of TES–PCM, as, to the best of our knowledge, the method has not yet been applied to high-fidelity simulations of such systems.

Compared to classical Eulerian approaches commonly used for TES–PCM simulations, PFEM offers several advantages that are particularly relevant in the presence of phase change and natural convection. As a fully Lagrangian method, PFEM naturally accounts for material advection, thereby avoiding the explicit discretization of convective terms in the momentum and energy equations, which are dominant in the liquid PCM and often require dedicated stabilization techniques in Eulerian formulations. Moreover, the continuous remeshing inherent to PFEM enables the spatial discretization to adapt dynamically to evolving thermal gradients and to the thickness of the mushy zone, allowing computational effort to be concentrated only where high resolution is required. This contrasts with fixed-mesh Eulerian methods, which typically rely on uniformly fine meshes to resolve the thinnest mushy layers, resulting in increased computational cost. On the other hand, the frequent remeshing in PFEM may hinder highly efficient parallelization compared to fixed-grid Eulerian solvers. Nevertheless, the improved flexibility in spatial discretization makes PFEM a competitive and well-suited approach for TES–PCM simulations.

It should be noted that PFEM is still a relatively young method, and efforts toward highly efficient parallel implementations are only recently emerging in the literature. Promising directions include GPU-based formulations (Zhang et al., 2021), which have demonstrated significant potential for large-scale and highly nonlinear problems. In contrast, the present PFEM implementation (Février, 2020) relies on a CPU-based framework that does not yet fully exploit parallel efficiency. Consequently, the objective of this work is not to provide a quantitative performance comparison against classical Eulerian approaches, but rather to demonstrate and validate PFEM as a promising and flexible strategy for the simulation of TES–PCM systems.

In this work, we build upon recent advances in PFEM for phase-change modeling to reach the current state of the art in TES–PCM simulations based on the enthalpy–porosity method. Specif-

ically, we rely on the implementation by Bobach et al. (2021), which was validated against the benchmark melting problem of a gallium block. This implementation has also been successfully employed in the simulation of welding processes (Fernández et al., 2024) and extended to model melt pools in additive manufacturing (Février et al., 2025). However, the strong thermal gradients in the phase-change region motivate the development of a new mesh adaptation criterion for PFEM, aimed at reducing the amount of elements without compromising accuracy of TES-PCM simulations.

The remainder of this manuscript is organized as follows. Section 2 describes the physical modeling of TES-PCM using PFEM. Section 3 presents the proposed mesh adaptation criterion, designed to capture the steep thermal gradients in the PCM while using a moderate number of elements. Section 4 validates the proposed PFEM model against experimental results from the literature, including a parametric optimization study in which we optimize the vertical position of an HCM fin, aiming to replicate and critically assess results reported in the literature.

2 The Particle Finite Element Method

The Particle Finite Element Method (PFEM), proposed by Idelsohn et al. (2004), was originally designed for the simulation of free-surface fluid flows. To achieve this, PFEM resorts to two techniques, FEM and efficient remeshing. At each time step, PFEM solves the governing equations using FEM in an updated Lagrangian framework, i.e., the nodes (or particles) that discretize the fluid are displaced at the end of the time step. The new nodal position may result in highly distorted and useless elements, so a remeshing must be performed. The most efficient strategy to date is to perform a Delaunay triangulation of all nodes (or particles) present in the model and then remove those elements that do not belong to the initial body. The element removal criterion classically used in PFEM is the alpha-shape algorithm (Edelsbrunner and Mücke, 1994), although methods based on the level-set have also been proposed (Fernández et al., 2023a).

A key advantage of PFEM is that it allows only the fluid of interest to be modeled, unlike classical CFD methods that require two-phase models to simulate also the air in case of free surface fluid flows. Other advantages of PFEM are the easy identification of fluid boundaries, the use of a mesh that is conformal at the fluid boundaries, and the possibility to capture the separation or merging of bodies throughout the simulation, i.e., capturing significant topological changes without difficulty, such as fluid splashing. These attractive numerical features of PFEM were later exploited in other applications, such as simulations of fluid-structure interactions, plasticity (Rodriguez et al., 2016), and simulation of melt pools (Février et al., 2025). See the work of Cremonesi et al. (2020) for a more expanded overview on the extensions of PFEM for simulating engineering problems.

An additional numerical advantage provided by PFEM is that during the remeshing process, it is possible to add or remove particles from the domain to maintain a desired spatial discretization. For example, Fernández et al. (2023a) increase the spatial resolution at the free surface, Rodríguez et al. (2017) near the rupture zone, Lacroix et al. (2024) at the fluid-structure interface, and Février (2020) in the phase change zone. The easy adaptation of space discretization has also been applied to confined flows by Falla et al. (2023), i.e. simulations without moving interfaces. In such a case, Falla et al. (2023) developed particle distribution criteria to spatially capture high velocity gradients. This same idea is adopted and adapted to the case of TES-PCM simulation in the present work. Details of our proposal are given in Section 3.

The system of equations to be solved with PFEM is the heat equation and the Navier-Stokes equations. In a Lagrangian framework and for an incompressible Newtonian fluid, the equations are:

$$\rho \frac{d\mathbf{v}}{dt} - \mu \Delta \mathbf{v} + \nabla \mathrm{p} = \rho \boldsymbol{b} + \boldsymbol{s} \tag{1a}$$

$$\nabla \cdot \mathbf{v} = 0 \tag{1b}$$

$$\rho c_{\mathrm{p}} \frac{dT}{dt} + \nabla \cdot \boldsymbol{q} = L \tag{1c}$$

where ρ is density, $\mathbf{v}$ is the velocity vector, t is time, μ is the dynamic viscosity, Δ is the Laplacian operator, ∇ is the gradient operator, p is the pressure, and $\boldsymbol{b}$ is the gravitational acceleration vector. Natural convection is accounted for by the Boussinesq approximation, i.e. the density in the body forces term is updated as a function of the temperature T. c_{p} is the specific heat capacity and $\boldsymbol{q}$ is the heat flux vector in the form of thermal conduction:

$$\boldsymbol{q} = -\kappa \nabla T \tag{2}$$

where κ is the thermal conductivity. The phase change in Eq. (1) is taken into account in the terms L and $\boldsymbol{s}$. The first one is the latent heat of fusion while the second one originates from the Carman-Kozeny equation and allows to shift the particle behaviour between the liquid and solid states. These terms are defined as:

$$L = -\rho \, \frac{df_l}{dT} \, \frac{dT}{dt} \, L_{\mathrm{m}} \tag{3a}$$

$$\boldsymbol{s} = c_{\mathrm{ck}} \, \frac{(1 - f_l)^2}{\epsilon_{\mathrm{ck}} + f_l^3} \mathbf{v} \tag{3b}$$

where L_{m} is the latent heat of fusion, f_l is the liquid fraction, and c_{ck} and ϵ_{ck} are user defined parameters, such that, c_{ck} must be large so that $\boldsymbol{s}$ results in a large number absorbing all the momentum when $f_l \to 0$, and ϵ_{ck} must be small to avoid affecting the momentum equation when $f_l \to 1$, but big enough to prevent numerical singularities when $f_l = 0$. The liquid fraction f_l, present in the L and $\boldsymbol{s}$ parameters, is defined as:

$$f_l = \begin{cases} 1 & \text{, for } T \geq T_{\mathrm{liq}} \\ \dfrac{T - T_{\mathrm{sol}}}{T_{\mathrm{liq}} - T_{\mathrm{sol}}} & \text{, for } T_{\mathrm{sol}} < T < T_{\mathrm{liq}} \\ 0 & \text{, for } T \leq T_{\mathrm{sol}} \end{cases} \tag{4}$$

Thus, if the particle temperature is higher than the liquidus temperature, T_{liq}, then $\boldsymbol{s}$ becomes zero and the flow is governed by the Navier-Stokes equations. If the temperature is lower than T_{liq}, the term becomes negative, penalising the flow by acting as a momentum sink to the point of consuming all the momentum when the temperature drops below T_{sol} (solidus temperature).

The Carman–Kozeny parameters, c_{ck} and ϵ_{ck}, are numerical regularization parameters. Their optimal values are problem-dependent and are known to vary with the characteristic length and time scales of the problem, as well as with the intensity of natural convection. Typical values reported in the literature dedicated to TES-PCM simulation range from 10^5 (Kalapala and Devanuri, 2021; Xu et al., 2021; Liu et al., 2024; Kang et al., 2025) to 10^7 (Safari et al., 2021; Garoosi et al., 2025) for c_{ck}, and around 10^{-3} for ϵ_{ck} (see references given for c_{ck} values). In practice, these parameters are chosen to be sufficiently large to effectively suppress velocities in the solid phase, while maintaining numerical stability and convergence of the nonlinear solver. For this reason, different values are adopted across the numerical examples considered in this work, following a calibration process aimed at ensuring robust convergence of the solution.

The Eqs. (1) are complemented with Dirichlet and Neumann boundary conditions, discretized in space with triangular and linear elements, and discretized in time using the Backward Euler time integration scheme. The Navier-Stokes equations are solved in a monolithic form in a velocity-pressure scheme using the PSPG (Pressure-Stabilizing Petrov-Galerkin) stabilisation. The system of Eqs. (1) is solved in a staggered scheme, where the heat equation is solved before the Navier-Stokes equation, this is done repeatedly until tolerance for convergence is satisfied for both equations. The reader is referred to the works of Fernández et al. (2023b) for a detailed explanation of time integration methods in PFEM; Cerquaglia (2019) for details of PSPG stabilization in PFEM; Février et al. (2025) for a detailed explanation of the staggered scheme for simulating thermo-fluids with phase change in PFEM; and Février (2020) for details on the numerical implementation of the code used in this work, named *PFEM3D*.

The problems addressed in this work do not include a free surface, so we do not use the alpha-shape criterion. This means that all elements of the Delaunay triangulation are accepted in the remeshing step of PFEM. However, we do use the two criteria that control the element size in PFEM, which are the removal of very close particles (to avoid agglomeration) and the addition of particles in sparse particle zones. These criteria are imposed according to the user-defined element size, denoted by h_{ele}, which is specified at the nodes. There are different algorithms in the PFEM literature for adding and removing nodes, but in this work we adopt the edge splitting approach (Falla et al., 2023; Lacroix et al., 2026), as it allows adapting element sizes at the boundaries of the domain. Thus, a particle (or node) is removed if it lies at a distance less than γh_{ele} from another particle, as shown by the blue nodes in Fig. 3. On the contrary, particles will be incorporated into the model at the edges of an element if its size exceeds $\Omega h_{\mathrm{ele}}^2$, as shown in the orange-hatched elements in Fig. 3. As is common in the literature, $\gamma = 0.4$ and $\Omega = 0.9$ in this work. The reader is referred to the works of Cerquaglia (2019) and Lacroix (2025) for a more in-depth analysis of the criteria for adding and removing particles.

It is worth noting that PFEM operates with nodal variables and first-order elements. Consequently, when new particles are introduced during remeshing, their state variables (temperature,

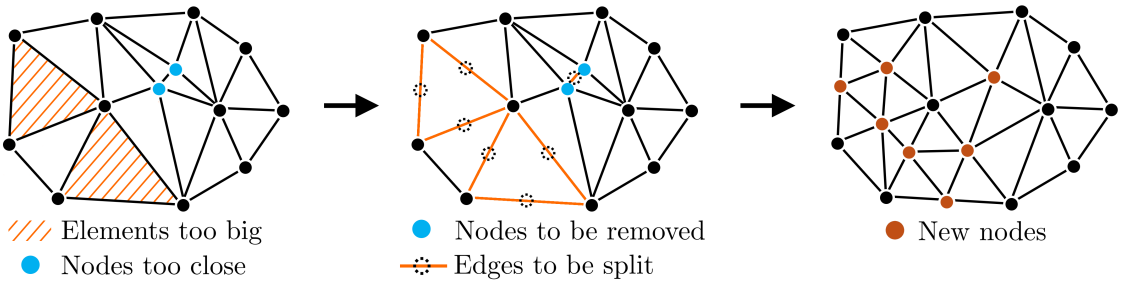

Figure 3: Illustration of the edge splitting remeshing algorithm (Lacroix et al., 2026) used in this work.

velocity, pressure) are initialized by linear interpolation from the particles defining the corresponding edge. Changes in mesh connectivity, as well as the insertion and removal of particles inherent to the remeshing process, may introduce a certain level of numerical diffusion. However, in practical PFEM applications, remeshing is not performed at every time step. In many implementations, the time step is chosen such that particle displacements between consecutive time steps remain moderate, in order to avoid the development of highly distorted elements, unless more advanced PFEM variants allowing for larger time steps are employed (e.g., see PFEM-2 proposed by Idelsohn et al. (2013)). As a result, significant mesh distortions typically develop only over some time steps, particularly in the absence of strong shear or vortex-dominated flows (Fritts and Boris, 1979). Consequently, remeshing is commonly applied only intermittently, which limits the accumulation of numerical diffusion. Moreover, particle insertion and removal usually occur in localized regions of the domain, so that the Delaunay triangulations before and after remeshing remain nearly identical away from these regions, thus limiting diffusion at the global level.

3 A new PFEM remeshing scheme for TES-PCM simulation

The PFEM model described above has already been validated for phase change simulation in the literature (Bobach et al., 2021), however it was performed for materials with high thermal diffusivity such as gallium. In this section, we show that current PFEM remeshing strategies are not suitable in the case of TES-PCM due to the low thermal diffusivity of the material subject to phase change, and therefore a new criterion must be developed.

In the PFEM literature, two methods are widespread for imposing element size. One is to define h_{ele} uniformly throughout the domain. That is, all nodes get the same size h_{ele}. The second method is to define h_{ele} based on the distance of nodes to the surface of interest. For example, in simulations with phase changes, it would be the shortest distance to the mushy zone, which is denoted by d_{MZ} in this work. Typically, a piecewise linear function is used to define $h_{\text{ele}}(d_{\text{MZ}})$, as follows:

$$h_{\text{ele}}(d_{\text{MZ}}) = \begin{cases} h_{\min}, & \text{if } d_{\text{MZ}} \leq d_{\min} \ , \\ \dfrac{h_{\max} - h_{\min}}{d_{\max} - d_{\min}}(d_{\text{MZ}} - d_{\min}) + h_{\min}, & \text{if } d_{\min} < d_{\text{MZ}} < d_{\max} \ , \\ h_{\min}, & \text{if } d_{\text{MZ}} \geq d_{\max} \end{cases} \tag{5}$$

where $h_{\min}$ is the minimum element size imposed in the mushy zone and up to a distance $d_{\min}$, and $h_{\max}$ is the maximum element size imposed at a distance $d_{\max}$. This function is also illustrated in Fig. 4a.

Distance-based mesh adaptation is very useful in simulations with moving interfaces, such as in the case of phase change, since it coarsens the discretization outside critical areas, thereby reducing computation time compared to a uniform mesh. To illustrate this, consider as an academic case, the small TES-PCM device of 15x20 mm^2 shown in Fig. 4b. This device presents an initial temperature of 25°C, while heat is incorporated by the left wall, which is at 60°C.

As mentioned above, PFEM has already been used to simulate phase changes, but in materials with high thermal diffusivity, which differs from the materials used in TES-PCM. For illustrative purposes, the academic TES-PCM device is filled with lauric acid and a fictitious material that matches the physical parameters of lauric acid, except for the latent heat of fusion and thermal conductivity, which are set to those of gallium. This produces a material with a thermal diffusivity 200 times greater than that of lauric acid, but with the same melting point for comparative purposes. Physical parameters of the simulated PCMs in this work are given in Table I. Lauric acid and gallium are chosen because they are used in the experimental studies (Gau and Viskanta, 1986; Kamkari and Shokouhmand, 2014) that we employed for model validation.

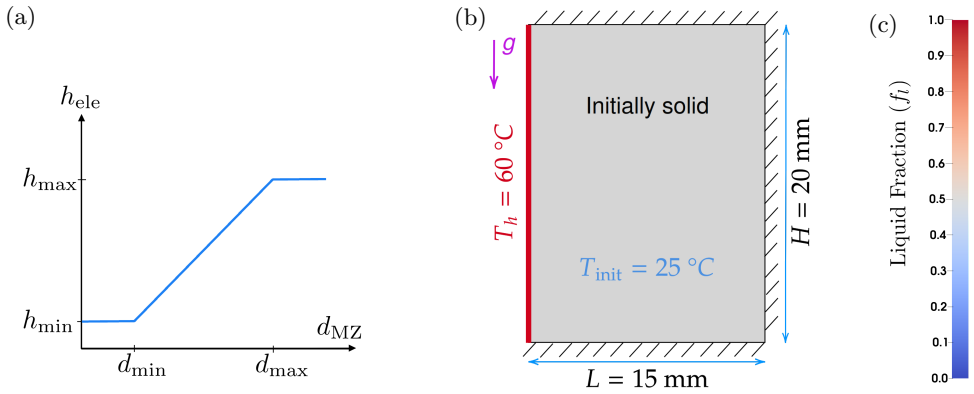

Figure 4: (a) The function that defines the element size based on the distance to the mushy zone. (b) The thermo-fluid problem with phase change used to illustrate the need for a new mesh adaptation criterion. (c) Color bar used in this work for the liquid fraction.

Table I: Thermophysical properties of lauric acid (Kamkari and Shokouhmand, 2014; Shokouhmand and Kamkari, 2013), gallium (Bobach et al., 2021), and paraffin (Xu et al., 2021), used in this work as PCM.

Property	Lauric acid solid / liquid	Gallium solid / liquid	Paraffin solid / liquid
Specific heat capacity (J/kgK)	2180 / 2390	381.5	2500
Melting temperature (°C)	43.5 / 48.2	29.63	47.51 / 48.51
Thermal conductivity (W/m K)	0.16 / 0.14	32.00	0.295
Density (kg/m^3)	940 / 885	6093	820
Dynamic viscosity (Pa s)	4.4×10^{-3}	1.81×10^{-3}	2.05×10^{-1}
Latent heat of fusion (kJ/kg)	187.21	80.16	210.00
Thermal expansion (1/K)	9.0×10^{-4}	1.2×10^{-4}	6.0×10^{-4}

The thermal charging process is simulated for both materials using different uniform spatial discretizations, ranging from h_{ele} = 0.2 mm to h_{ele} = 3.2 mm, with a constant time step of 0.03 seconds for all discretizations. In each simulation, the total amount of melted PCM over the simulation is analysed. Note that the melting rate is examined throughout this work, which is a conventional approach in the charging analysis of TES-PCM devices. In addition, simulation snapshots are provided in this work showing, in most cases, the liquid fraction in the domain, whose color bar is shown in Fig. 4c.

The thermal charging processes using the fictitious material and the lauric acid are shown in Figs. 5a and 5b, respectively. Here, a simulation challenge can already be observed, because the lauric acid exhibits a significantly longer charging time than the fictitious material, with only two physical parameters differing: thermal conductivity and latent heat of fusion. Another aspect to consider is that lauric acid proves to be more sensitive to element size compared to the material with high thermal diffusivity. In fact, the melted-PCM curves are rather similar for h_{ele} equal to 0.2, 0.4, and 0.8 mm in the case of the fictitious material, and all discretizations converge at practically the same total melting time. In contrast, coarse discretizations (1.6 and 3.2 mm) do not allow numerical convergence of the problem in the case of lauric acid. Furthermore, the total charging times are highly dependent on the discretization. The reason for this is the presence of significantly thin mushy layers in lauric acid, which must be discretized with about 5 elements in the thickness for a good resolution and accuracy according to the study of Garoosi et al. (2025). Table. II shows that this is only achieved with h_{ele} = 0.2 mm in the case of lauric acid.

Table. II shows snapshots of the simulated TES-PCM devices at 40% of melted PCM. It can be seen that the mushy layer in the case of lauric acid is considerably thinner than that of the fictitious material, which requires higher spatial resolution to be captured correctly. In this context, the remeshing strategy based on the distance to the mushy zone is interesting, as it allows the discretization to be concentrated only in the zone of interest.

Next, the academic problem is solved for lauric acid using $h_{ele}(d_{MZ})$. To correctly capture the mushy zone, h_{min} = 0.2 mm is used up to a distance d_{min} = 0.2 mm. The maximum size is h_{max} = 2 mm and is applied from a distance d_{max} = 6 mm. In addition, it is chosen to keep a small element size at the no-slip boundaries to avoid compromising the accuracy of the flow. Practically

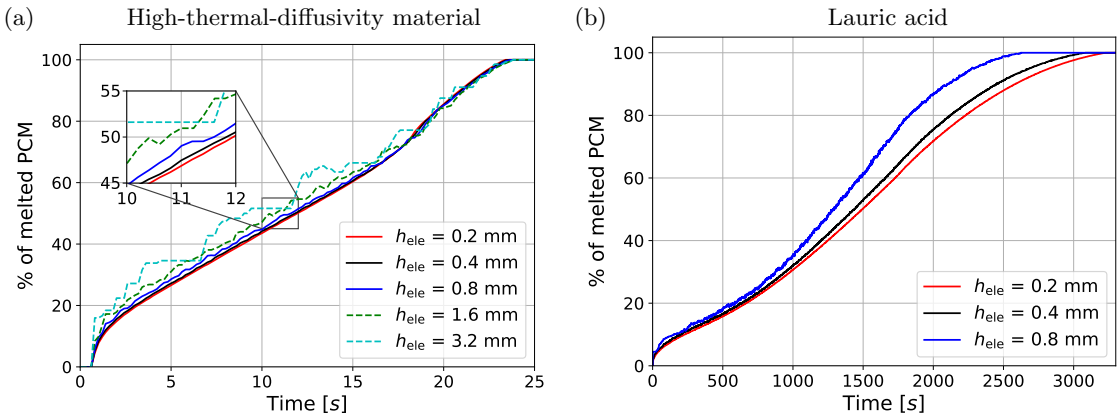

Figure 5: Evolution of the thermal charging process of the TES-PCM equipment illustrated in Fig. 4b. The PCM used is (a) a fictitious material similar to lauric acid but with a thermal diffusivity 200 times greater, and (b) lauric acid. Different curves are generated for different spatial discretizations with uniform element size.

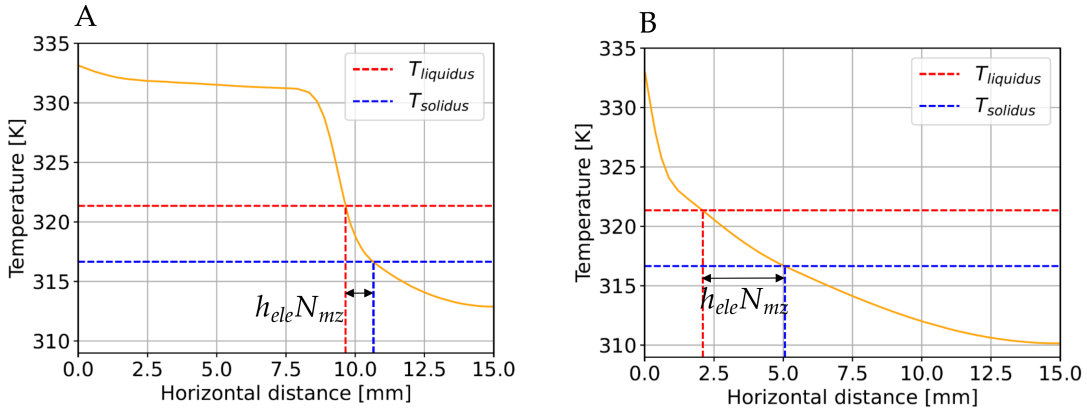

Figure 6: Temperature profile illustration at lines "A" and "B" depicted in Table II.

speaking, these boundaries can be considered as the limits of the mushy zone in the definition of $h_{\text{ele}}(d_{\text{MZ}})$. However, the solid phase of the PCM is restricted in movement, so refinement with respect to non-slip boundaries is applied only in the fluid phase ($f_l = 1$).

The last column of Table. II shows a simulation snapshot using $h_{\text{ele}}(d_{\text{MZ}})$. Here, it is clearly visible that the total number of elements is considerably lower than in the case of uniform element size, which implies a considerable computational benefit in the context of PFEM. However, it should be noted that a large number of elements are still used to discretize the mushy zone, especially in the lower part of the model. This is a consequence of natural convection: as the left wall is heated, the melted liquid becomes less dense and rises, creating a convective loop that transports heat more efficiently to the upper part of the domain. As a result, melting progresses more slowly in the lower region, where heat is transferred mainly by conduction, leading to a thicker mushy zone since the thermal gradient driving the phase change moves more slowly in that area. This phenomenon can result in a large number of elements within the mushy zone, allowing for further mesh adaptation optimization.

Our proposal focuses on the mushy zone and seeks to set an element size proportional to the thickness of the mushy zone. The goal is to ensure a minimum number of elements through the thickness to guarantee numerical convergence in thin mushy zones, but to limit the number of elements when the mushy zone becomes thicker. To do this, we use the thermal gradient within the mushy zone as a refinement criterion. The idea can be easily explained using the temperature profile across the width of the mushy zone, as shown in Fig. 6. The goal is to divide the mushy zone across the thickness into N_{mz} elements. Assuming that the thermal gradient in the mushy zone is constant, then we can write:

$$\|\nabla T\| \approx \frac{T_{\text{liq}} - T_{\text{sol}}}{h_{\text{ele}}\, N_{\text{mz}}} \implies h_{\text{ele}} \approx \frac{T_{\text{liq}} - T_{\text{sol}}}{\|\nabla T\|\, N_{\text{mz}}} \tag{6}$$

The above expression allows us to approximate the size of the element based on the temperature gradient, exclusively within the mushy zone. However, the expression must be complemented with

Table II: Snapshots of the problem shown in Fig. 4b, using lauric acid as PCM and the same material but with a thermal diffusivity 200 times larger. The snapshots are taken at 1250 seconds in lauric acid, and at 9 seconds in the other material. The fifth column shows a result for a mesh obtained with the distance-based strategy, and the rest using a uniform element size. Color bar of liquid fraction is given in 4c.

	High thermal diffusivity		Lauric Acid		
	$h_{\text{ele}} = 0.8$ mm	$h_{\text{ele}} = 0.2$ mm	$h_{\text{ele}} = 0.8$ mm	$h_{\text{ele}} = 0.2$ mm	$h_{\text{ele}}(d_{\text{MZ}})$
Liquid fraction	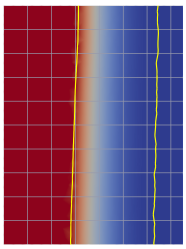	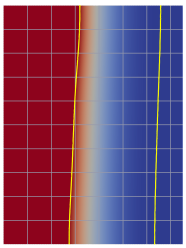	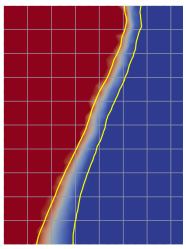	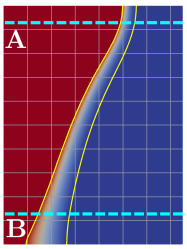	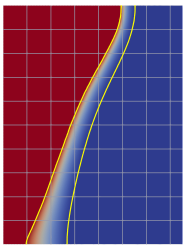
Mesh	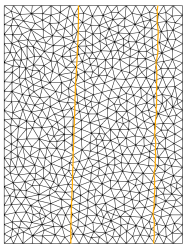	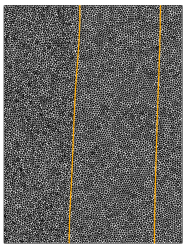	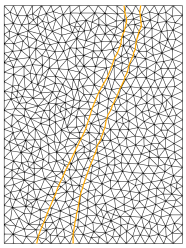	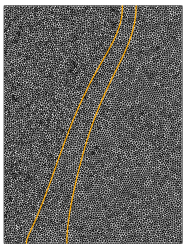	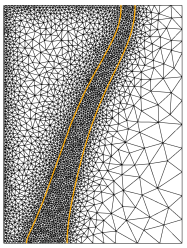
	1246 elements 668 nodes	20302 elements 10327 nodes	1280 elements 685 nodes	20338 elements 10345 nodes	6327 elements 3294 nodes

lower and upper limits, denoted as $h_{\text{mz,min}}$ and $h_{\text{mz,max}}$, respectively. The reason is that, if the mushy zone becomes considerably wide, the thermal gradient may be small enough to generate large elements within the mushy zone, and conversely, large thermal gradients may lead to elements of nearly zero size. Thus, within the mushy zone, we impose the following characteristic element size:

$$h_{\text{ele}}(\|\nabla T\|) = \min\left(\max\left(\frac{T_{\text{liq}} - T_{\text{sol}}}{\|\nabla T\|\, N_{\text{mz}}}\ ,\ h_{\text{mz,min}}\right)\ ,\ h_{\text{mz,max}}\right) \tag{7}$$

Outside the mushy zone, our implementation uses distance-based remeshing, meaning that our proposal reads as follows:

$$h_{\text{ele}}(d_{\text{MZ}}, \|\nabla T\|) = \begin{cases} h_{\text{ele}}(\|\nabla T\|) & , \quad \text{if} \quad 0 < fl < 1\ , \\ h_{\text{ele}}(d_{\text{MZ}}) & , \quad \text{otherwise} \end{cases} \tag{8}$$

Next, the academic problem is solved for lauric acid using the same distance-based remeshing criterion, $h_{\text{ele}}(d_{\text{MZ}})$, and our contribution, $h_{\text{ele}}(d_{\text{MZ}}, \|\nabla T\|)$. For the latter, we set $N_{\text{mz}} = 5$, $h_{\text{mz,min}} = 0.2$ mm, and $h_{\text{mz,max}} = 0.4$ mm. Fig. 7a compares the meshes obtained with $h_{\text{ele}}(d_{\text{MZ}})$ and $h_{\text{ele}}(d_{\text{MZ}}, \|\nabla T\|)$, both capturing the same physical time 1250 seconds, as done in Table II. For that snapshot and compared to the distance-based technique ($h_{\text{ele}}(d_{\text{MZ}})$), a reduction of about 21 % in the amount of elements is obtained with the proposed coarsening technique for the mushy zone, and a remarkable reduction of about 75 % with respect to the uniform mesh. This reduction in mesh elements will translate into a significant decrease in CPU time. The total amount of elements throughout the simulation is illustrated in Fig. 7b, and it can be seen that globally, the remeshing based on the thermal gradient magnitude is always reduced in the amount of elements, with a peak reduction of about 34 % (see blue curve in Fig. 7b).

Certainly, using a coarser mesh may affect the numerical resolution of the solution. However, in the proposed strategy, mesh coarsening is primarily applied in regions characterized by low thermal gradients, low velocity gradients (away from no-slip boundaries), and within the solid zone where no displacements occur. As a result, the impact of mesh coarsening on the global solution can be considered negligible compared to the computational benefit gained. This is illustrated in Fig. 8a, which compares the evolution of the total melted volume obtained with the three remeshing strategies. A maximum deviation of approximately 2.0 % in the melted volume is observed between the proposed remeshing strategy and the uniform mesh (see green curve in Fig. 8b).

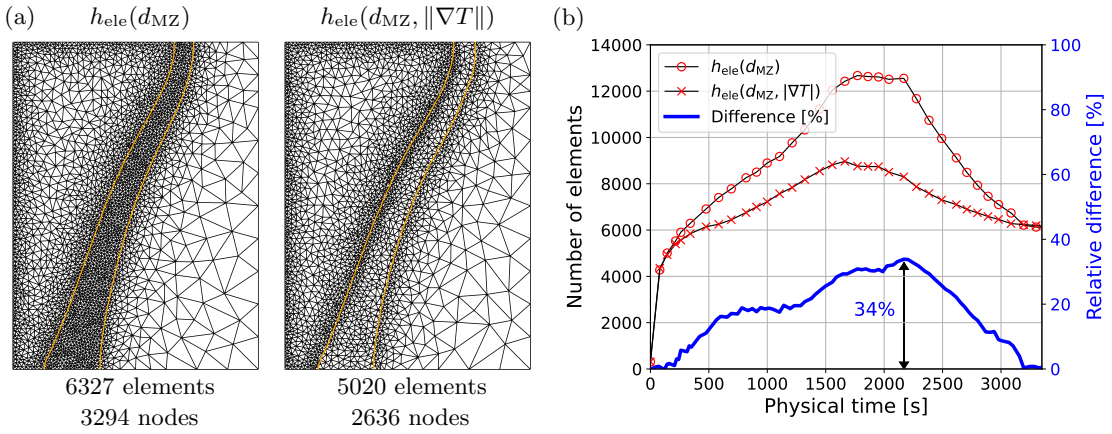

Figure 7: (a) Solutions to the problem in Fig. 4b obtained with two remeshing criteria: the classic distance-based criterion and the proposed one that also includes the thermal gradient as a criterion inside the mushy zone. The orange lines delimit the boundaries of the mushy zone. (b) The number of elements throughout the simulation and the relative difference between the two remeshing methods.

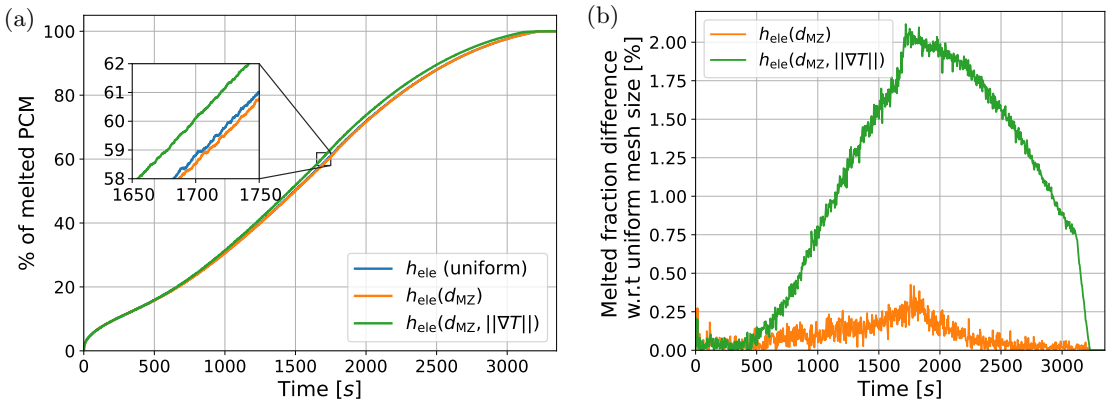

Figure 8: (a) Comparison of the amount of melted PCM over time using the three different remeshing strategies: uniform size of 0.2 mm, based on distance to the mushy zone, and the one that also includes a coarsening within the mushy zone. (b) The relative difference with respect to the solution that uses a uniform mesh size.

Having introduced the new remeshing criterion for PFEM aimed at TES-PCM simulations, the following section focuses on validating it.

4 Validation and numerical examples

To validate our PFEM implementation within the TES-PCM framework, including the newly introduced mesh adaptation strategy based on the thermal gradient, we rely on the experimental works of Gau and Viskanta (1986), and Kamkari and Shokouhmand (2014). The first is widely used in the phase change simulation literature and consists of melting a block of gallium initially in solid state. Given its high thermal diffusivity, this problem allows us to compare the $h_{ele}(d_{MZ})$ and $h_{ele}(d_{MZ}, \|\nabla T\|)$ remeshing criteria. The second involves the melting of lauric acid, a material typically used as a PCM for TES. For validation, two configurations are considered: with and without a fin located at half the height of the TES device. Finally, our PFEM implementation for TES-PCM is verified in a fin positioning optimization problem, seeking to replicate the results of Xu et al. (2021).

4.1 Gallium melting problem

Following the problem setting of Bobach et al. (2021), the model for the gallium problem retains the same geometric form as the one used in the previous section. Thus, using Fig. 4b as a reference, the height (H) in this case is 63.5 mm and the length (L) is 88.9 mm. The initial temperature is now 301.3 K and the temperature of the left wall is 311.0 K. The thermophysical properties of

Table III: Numerical parameters used in the problems presented in Section 4. Parameters for $h_{\text{ele}}(d_{\text{MZ}})$ and $h_{\text{ele}}(\|\nabla T\|)$ are given in mm.

	Carman-Cozeny		$h_{\text{ele}}(d_{\text{MZ}})$				$h_{\text{ele}}(\|\nabla T\|)$		
Section	ϵ_{ck}	c_{ck}	h_{min}	h_{max}	d_{min}	d_{max}	N_{mz}	$h_{\text{MZ.min}}$	$h_{\text{MZ.max}}$
4.1	10^{-8}	10^{7}	0.4	4.0	0.4	10.0	5	0.4	0.8
4.2	10^{-3}	10^{6}	0.2	2.0	0.2	6.0	5	0.1	1.0
4.3	10^{-2}	10^{7}	0.02	0.12	0.02	0.20	5	0.01	0.06

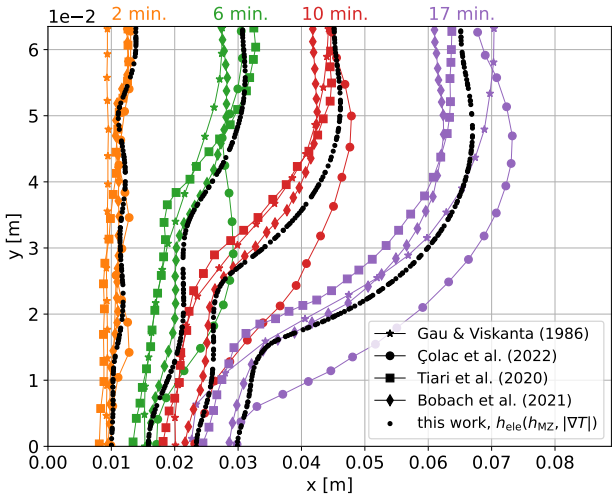

Figure 9: Melting fronts of the gallium melting problem.

the simulated material are summarized in Table I. These are chosen phase-independent as done in the reference literature (Çolak et al., 2022; Bobach et al., 2021; Tiari et al., 2021). Since gallium is a pure metal, the melting point occurs at a fixed temperature, i.e., $T_{\text{liq}} = T_{\text{sol}}$. However, it is convenient to smooth the transition to avoid a Heaviside function in the definition of the liquid fraction f_l. In this work, $T_{\text{liq}} - T_{\text{sol}} = 0.5$K and a constant time step of 0.02 s is used. Carman-Kozeny and remeshing parameters are given in the first row of Table III.

Fig. 9 summarizes the obtained results. There, different melting fronts reported in the literature are included, either obtained through experiments (Gau and Viskanta, 1986) or numerical simulations (Çolak et al., 2022; Bobach et al., 2021; Tiari et al., 2021). Four different times are reported in the graph (2, 6, 10, and 17 minutes), which are distinguished by color. To facilitate graphical comparison, the fronts obtained in this work are shown with black dots. Fig. 9 reports results obtained only with $h_{\text{ele}}(d_{\text{MZ}}, \|\nabla T\|)$, as they are practically identical to those obtained with $h_{\text{ele}}(d_{\text{MZ}})$. This can be seen in Fig. 9, which shows comparative snapshots around the melting fronts at 6 (Fig. 10a) and 17 (Fig. 10b) minutes.

It can be observed that the results obtained in this work are consistent with those reported in the literature, and closely match those of Bobach et al. (2021), who also employed the PFEM method. The results further show that the adaptation of the remeshing procedure proposed here for PFEM does not alter the outcomes obtained with the classical approach, which defines element size solely based on the distance to the mushy zone, as done by Bobach et al. (2021). This is because the element size is modified only within the mushy zone, i.e., $h_{\text{ele}}(d_{\text{MZ}})$ and $h_{\text{ele}}(d_{\text{MZ}}, \|\nabla T\|)$ yield the same element size outside this region. This subtle modification allows for a significant reduction in the number of nodes and elements discretizing the model, especially when the mushy zone becomes relatively thick, as illustrated in Fig. 10b and Fig. 11a. For this particular problem, a 25% reduction in total computation time is achieved, primarily due to a decrease in the cost of solving the governing equations (momentum and heat), as shown in Fig. 11b.

It is worth noting that the experimental data reported by Gau and Viskanta (1986) are subject to several sources of uncertainty that may partly explain the observed discrepancies in the melting-front position. Although the experimental set-up is carefully designed to approximate adiabatic boundary conditions, perfectly adiabatic walls cannot be achieved in practice, whereas such conditions are assumed in the numerical model. In addition, the presence of a large number

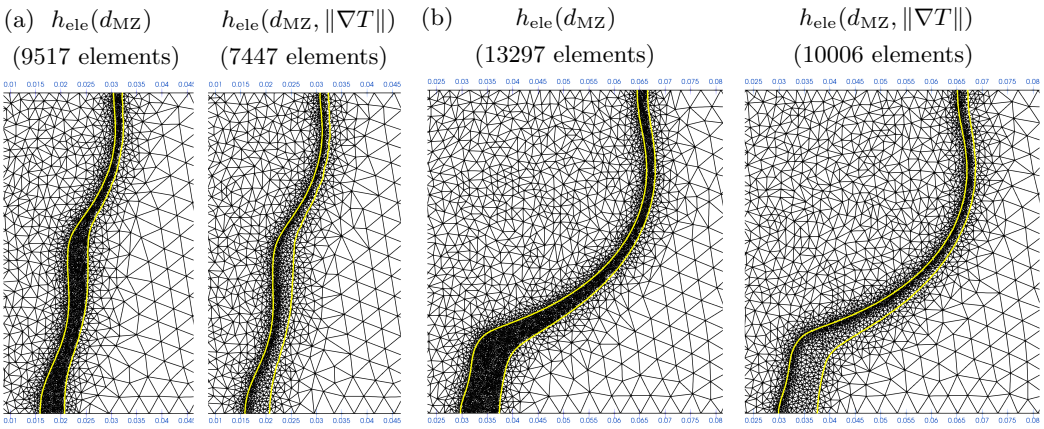

Figure 10: Snapshots of the gallium melting problem using two remeshing strategies, $h_{ele}(d_{MZ})$ and $h_{ele}(d_{MZ}, \|\nabla T\|)$, at times (a) 6 minutes and (b) 17 minutes.

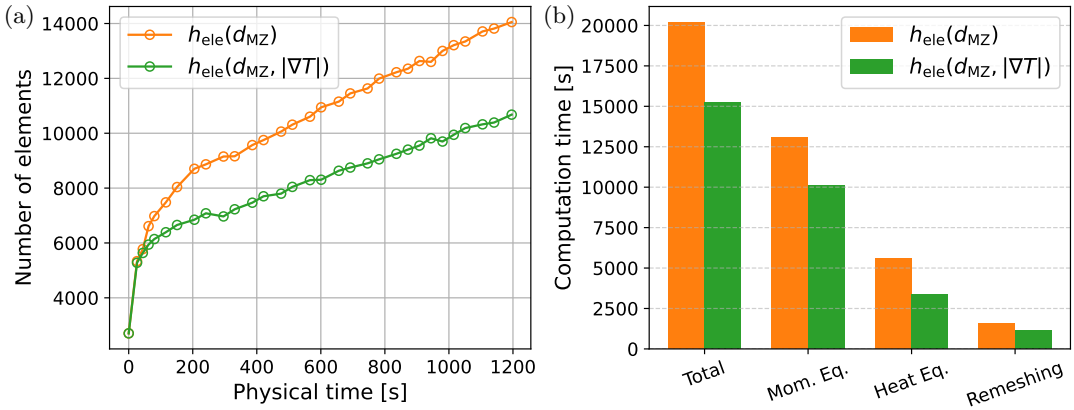

Figure 11: Computational performance of the two remeshing strategies analyzed in the gallium melting problem. (a) The total number of elements throughout the simulation and (b) the total simulation time including the three most time consuming tasks in our PFEM implementation. Computation time was measure using our PFEM implementation, executed in parallel using 4 processors, in an Intel(R) core(TM) i9-10900X CPU@3.70GHz station. Details about our PFEM3D code routines are given in (Lacroix, 2025).

of thermocouples embedded in the gallium, due to their high thermal conductivity, may locally perturb the temperature field and influence the measured position of the melting interface. Further uncertainties are related to the cavity filling procedure, since gallium must be liquefied before pouring, making it difficult to avoid the entrainment of air bubbles, which may subsequently migrate during heating and affect the experimental observations. Similar discrepancies between numerical predictions and experimental measurements have also been reported in previous PFEM studies (Bobach et al., 2021), particularly near the upper region of the cavity, where effects such as imperfect contact between the liquid gallium and the top wall due to shrinkage have been suggested as a possible explanation. Overall, the present results remain within the range of experimental and numerical variability reported in the literature, and the agreement observed can therefore be considered satisfactory.

A final parametric sensitivity study is conducted to conclude the gallium melting benchmark, focusing on the Carman–Kozeny parameters and the proposed remeshing strategy. Fig. 10 shows the melting fronts at 6 minutes of physical time for different values of ϵ_{ck}, c_{ck}, and the maximum element size in the mushy zone, $h_{MZ.max}$, while all remaining parameters are kept identical to those reported in Table III.

Fig. 12a shows the melting fronts obtained for different values of the Carman–Kozeny regularization parameter ϵ_{ck}. The results exhibit negligible sensitivity, with differences limited to localized regions and below approximately 1 mm, indicating that the solution is largely insensitive to ϵ_{ck} as long as sufficiently small values are employed. Fig. 12b illustrates the influence of the Carman–Kozeny penalization coefficient c_{ck}. A moderate sensitivity is observed, with larger deviations in the melting-front position as c_{ck} decreases. Lower values of c_{ck} weaken the momentum penalization in the mushy and solid regions, allowing higher velocities and greater convective heat transport, which leads to an accelerated melting process. Finally, Fig. 12c highlights the sensitivity of the solution to the maximum element size allowed within the mushy zone, $h_{MZ.max}$.

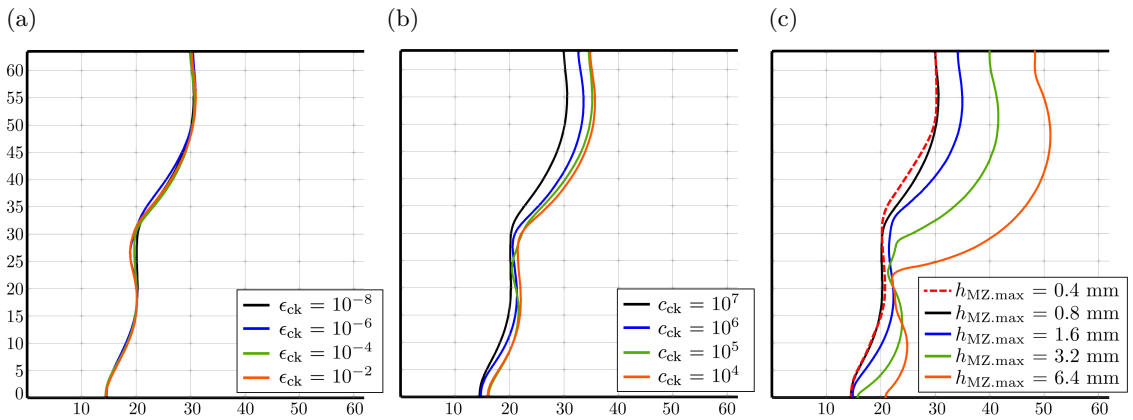

Figure 12: Melting fronts of the gallium benchmark at a physical time of 6 minutes obtained from the parametric sensitivity analysis. (a) Influence of the Carman–Kozeny regularization parameter ϵ_{ck}. (b) Influence of the Carman–Kozeny penalization coefficient c_{ck}. (c) Influence of the maximum element size allowed within the mushy zone, $h_{MZ.max}$. All remaining parameters are kept identical to those reported in Table III.

Results include the melting front for $h_{MZ.max} = 0.4$ mm, which results in the reference remeshing strategy $h_{ele}(d_{MZ})$, while $h_{MZ.max} = 0.8$ mm corresponds to $h_{ele}(d_{MZ}, \|\nabla T\|)$ as reported in Table III. Higher values of $h_{MZ.max}$ are also reported for the sensitivity analysis (1.6 mm, 3.2 mm, and 6.4 mm). Increasing $h_{MZ.max}$ results in a significant acceleration of the melting front, with deviations reaching several millimeters for coarse discretizations. This behavior can be attributed to an under-resolution of the steep thermal gradients within the mushy zone, which increases numerical diffusion and effectively reduces the thermal resistance of the phase-change region.

4.2 Charging simulation of a TES device

Having validated our proposed remeshing strategy for the mushy zone in the gallium melting problem, we now aim to validate it for the simulation of TES systems based on phase change materials (PCM). To this end, we use the results published by Kamkari and Shokouhmand (2014), who reported data for the charging process of a TES unit using lauric acid, both with and without aluminium fins.

The geometry of the present problem is the same as that shown in Fig. 4b, but with a height of 120 mm and a length of 50 mm. Compared to the gallium melting problem, the present one has a similar size. However, the physical simulation time is now 60 minutes, i.e., three times longer than in the gallium problem. In addition, a time step 4 times smaller is needed. Therefore, our proposed remeshing scheme $h_{ele}(d_{mz}, \|\nabla T\|)$ with reduced computational demand results attractive for solving this problem.

Two TES–PCM configurations are simulated here: one without fins and one equipped with a single fin. In both cases, the initial temperature is 25 °C and the hot wall is set at 70 °C. According to Kamkari and Shokouhmand (2014), the fin has a thickness of 4 mm, a length of 25 mm and it is positioned horizontally, with one end attached to the hot wall at mid-height. The density, thermal conductivity and specific heat capacity of the fin are, 2719 kg/m^3 , 202 W/m K , 87 J/kg K , respectively. In the PFEM context, the fin is fixed in all its degrees of freedom and it is not included in the momentum equation nor submitted to remeshing, i.e., it is only considered in the heat equation. Carman-Kozeny and remeshing parameters are given in the second row of Table III, and a constant time step of 0.005 s is used.

Graphical comparisons across the fifty first minutes of charging are illustrated for the case without fin in Table IV and with fin in Table V. It can be seen that in both cases, our model correctly captures the global shape of the melting front. Fig. 13 compares the total amount of melted PCM obtained experimentally and numerically, and reflects also the good correlation between the numerical and experimental results.

It is important to note the strong thermal gradient that occurs in the upper part of the model, which is due to efficient convective heat transfer, resulting in extremely narrow mushy zones. As can be seen in Fig. 14, our adaptive remeshing scheme allows us to accommodate a number of elements close to that provided through N_{mz}, enabling a locally refined discretization of the mushy zone. In particular, the mesh in Fig. 14 contains 39165 elements and 20121 nodes in total. In this mesh, approximately 20% of the elements (and nodes) are concentrated in the hot wall, 12%

Table IV: Evolution of the melting front of a TES device operating with lauric acid as PCM. The first row shows experimental snapshots from the work of Kamkari and Shokouhmand (2014), while the second row contains results from our PFEM simulation using the proposed remeshing strategy, i.e., $h_{\text{ele}}(d_{\text{MZ}}, \|\nabla T\|)$.

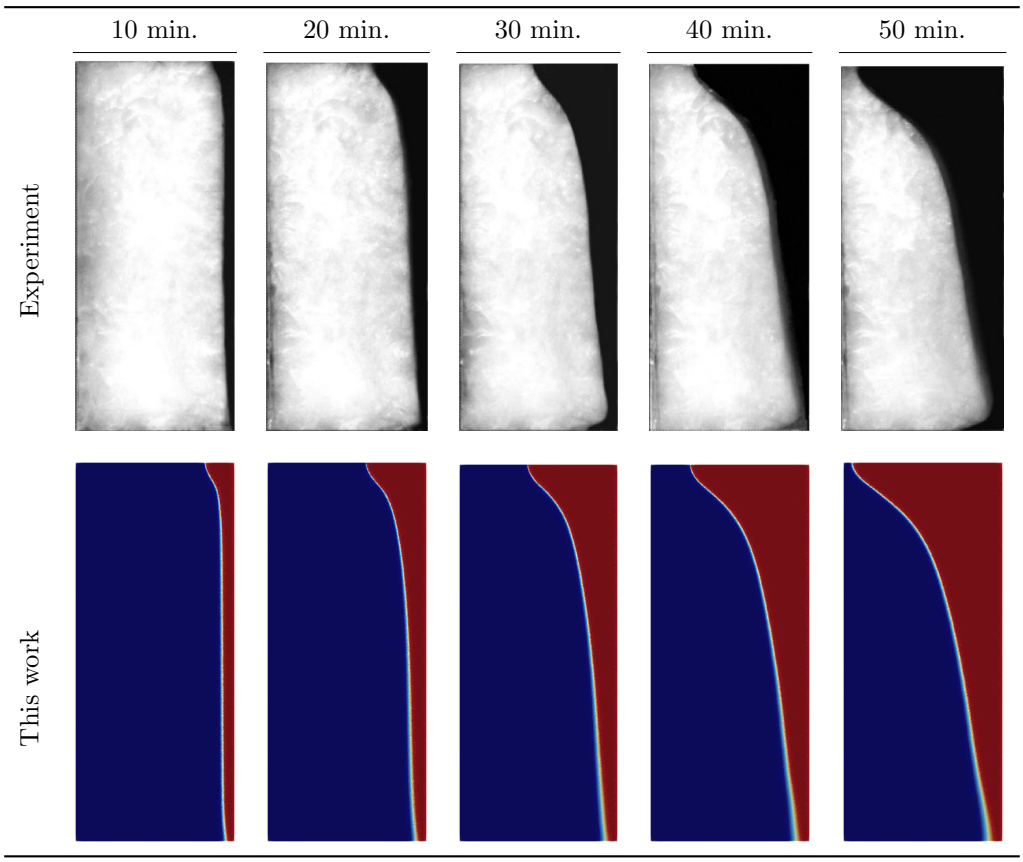

Table V: Evolution of the melting front of a TES device operating with lauric acid as PCM and equipped with an aluminium fin. The first row shows experimental snapshots from the work of Kamkari and Shokouhmand (2014), while the second row contains results from our PFEM simulation using the proposed remeshing strategy, i.e., $h_{\text{ele}}(d_{\text{MZ}}, \|\nabla T\|)$.

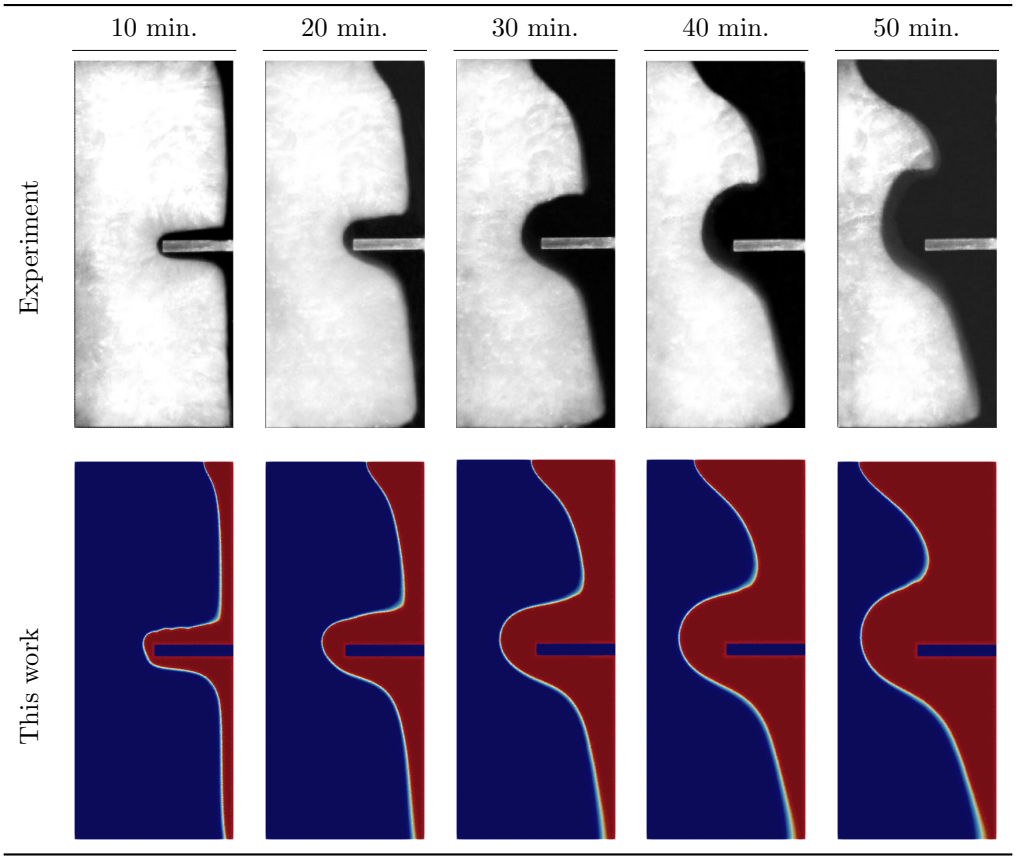

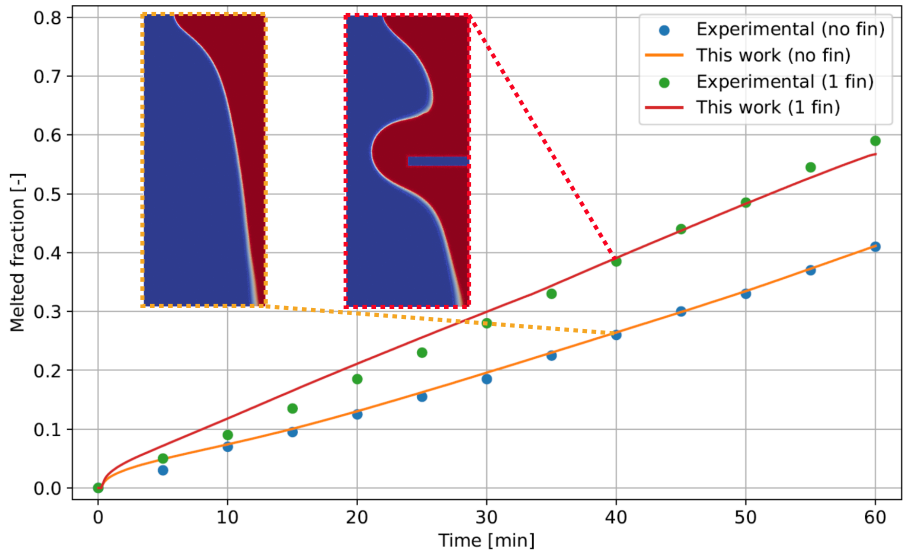

Figure 13: Evolution of the melted fraction with time, for both the experimental and numerical results.

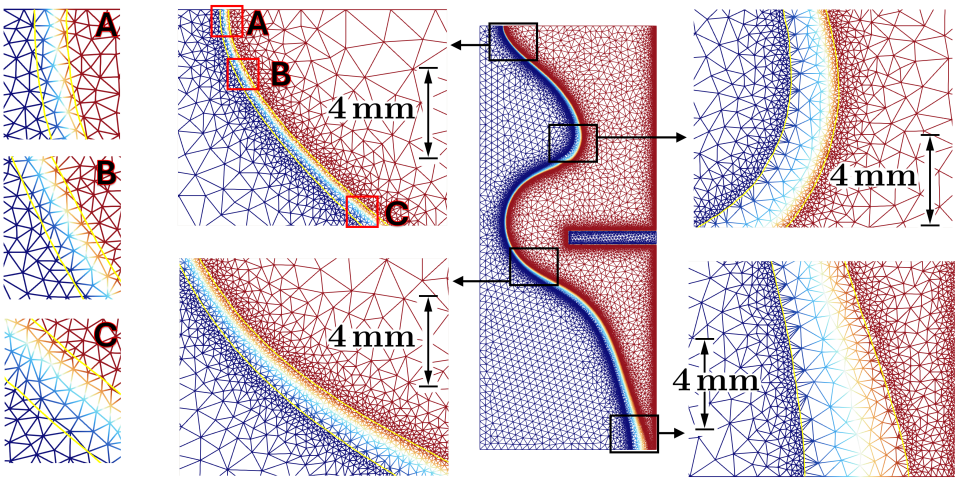

Figure 14: Mesh and liquid fraction of the TES device equipped with one fin after 50 minutes of charging. A 4 mm segment is placed for reference.

in the fin, 20% in the mushy zone ($0 < f_l < 1$), 19% in the liquid region adjacent to the mushy zone ($f_l = 1$), 18% in the solid region adjacent to the mushy zone ($f_l = 0$), and the remaining 11% in areas farther from the mushy zone, fin, and hot wall. These statistics were obtained using Paraview post-processing tools, considering a 3 mm distance around the aforementioned regions. In summary, in the snapshot of Fig. 14, which corresponds to one of the largest mushy layers in the simulation, about 57% of the elements are devoted to the discretization of the mushy region. Clearly, a uniform discretization within the mushy zone would result in a significantly larger number of elements.

Despite the overall good agreement between numerical predictions and experimental observations, some localized differences can be identified in the experimental images. In particular, a thin liquid layer advancing along the bottom wall can be observed, which is not present in the numerical results. This discrepancy can be attributed to experimental effects that are not explicitly modelled in the numerical framework. In particular, the numerical model assumes perfectly adiabatic conditions on the non-heated walls, whereas in practice a small amount of heat conduction through the enclosure walls is unavoidable. Such parasitic heat fluxes are expected to have a more noticeable impact near the bottom region of the cavity, where heat transfer is predominantly conductive and natural convection is weak. In contrast, in the upper region of the cavity, heat transfer is dominated by buoyancy-driven convection, which tends to mask the influence of small deviations from ideal adiabatic conditions. As a result, the experimentally observed "liquid tongue" along the bottom wall is likely associated with non-ideal boundary conditions rather than with limitations

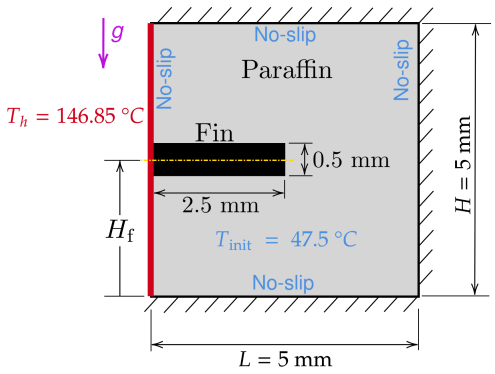

Figure 15: Model used by Xu et al. (2021) to perform the optimization of the fin position.

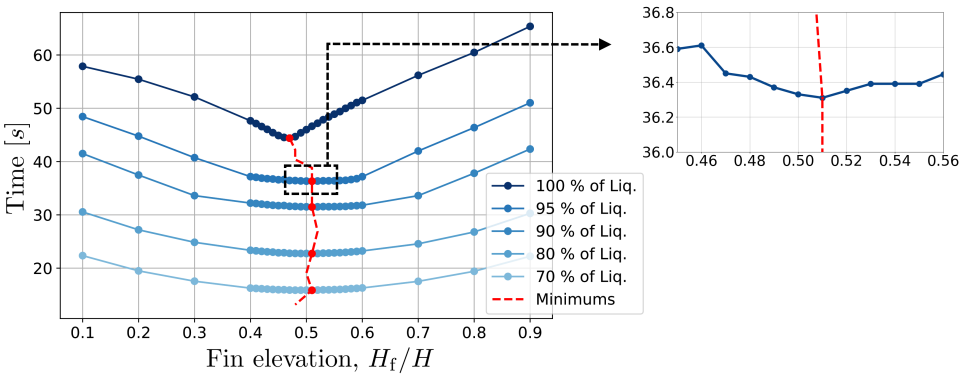

Figure 16: Melting time of paraffin for different vertical position of a cooper fin placed inside a TES device of 5×5 mm^2.

of the numerical model.

4.3 Fin position optimization of a TES-PCM using PFEM

Having validated the Particle Finite Element Method (PFEM) for the simulation of TES–PCM systems, including our contribution aimed at reducing the number of elements required to discretize the mushy zone, we now proceed to verify its performance in a practical application. The selected case concerns the optimization of the vertical placement of a fin, as presented by Xu et al. (2021). In their work, the authors employed a genetic algorithm to determine the optimal fin position that minimizes the charging time of the TES–PCM, with system performance evaluated through numerical simulations based on the enthalpy–porosity model using Ansys software. In contrast, the present study does not perform an optimization but rather generates a performance curve obtained using our PFEM model equipped with the proposed adaptive remeshing strategy.

The model of the TES device to be optimized is illustrated in Fig. 15, where H_f is the parameter to be optimized. Paraffin is used as PCM, whose physical properties are given in Table I. Copper is used as fin, with density, thermal conductivity and specific heat capacity equal to 8978 kg/m^3 , 387.6 W/m K and 381 J/kg K , respectively. Carman-Kozeny and remeshing parameters are given in the third row of Table III, and a constant time step of 0.001 s is used.

To construct the performance curve, a total of 27 simulations were carried out with variations in the vertical position of the fin. Specifically, 9 simulations were performed at increments of one-tenth of the model height, starting from 0.5 mm (0.1 H) up to 4.5 mm (0.9 H). The remaining eighteen simulations were conducted to increase the resolution of the curve around the mid-height region (0.5 H), which was reported as the optimal position by Xu et al. (2021). In this range, the fin height was varied with a step of 0.01 H, from 0.4 H to 0.6 H. On average, each simulation took approximately 420 seconds on the computer described in the caption of Fig. 11, using 8 processors. In total, 11340 seconds of computational time were required to construct the performance curve.

The obtained results are presented in Fig. 16. The abscissa represents the normalized fin height (H_f/H), while the ordinate shows the time required to reach a given percentage of melted PCM volume with respect to the total. The plot includes five performance curves corresponding to the times needed to achieve 70%, 80%, 90%, 95%, and 100% melting of the PCM. The red dashed curve indicates the optimal fin position for other melting fractions.

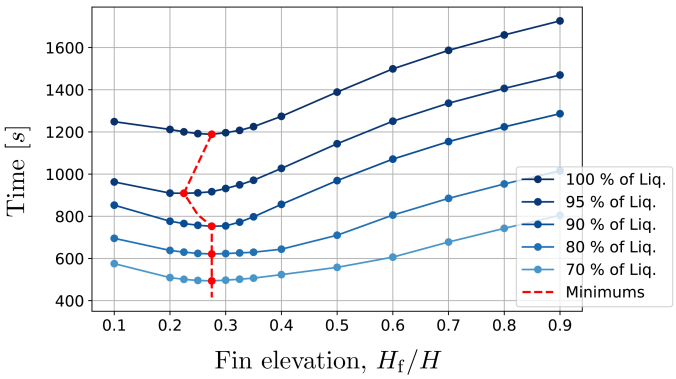

Figure 17: Melting time of paraffin for different vertical position of a cooper fin placed inside a TES device of 50×50 mm^2.

For all charging levels, the fin position that minimizes the charging time lies in the vicinity of 0.5 H. The performance curve is also observed to be smooth and convex, differing slightly from the results reported by Xu et al. (2021). In particular, our model predicts an optimal fin height of 0.47 H, which is relatively close to the 0.42 H obtained by the authors. However, it should be noted that the problem proposed by Xu et al. (2021) is significantly small and not fully representative of a real TES–PCM system. In fact, the total charging times do not exceed one minute, and the performance differences associated with fin position are on the order of 0.25 seconds near the optimal region, as shown in Fig. 16, i.e., a practically negligible amount. Moreover, the authors optimized their design based on the total charging time of the TES unit. However, in practical applications, TES–PCM systems are rarely charged to 100%, for two main reasons: (1) the temperature gradient decreases considerably as the PCM approaches complete melting, which greatly slows down heat transfer. For example, in the optimal design of the present problem, 34% of the total charging time is required to go from 90% to 100% of melted PCM. (2) Charging the TES–PCM unit to full capacity may cause local overheating and excessive thermal expansion, potentially compromising the system's integrity.

Regardless of the chosen charging level, Fig. 16 shows that the optimal fin position remains close to mid-height. This reflects that heat transfer in Xu's problem is mainly driven by conduction, due to the very short charging times resulting from the small model size. To support this observation, a new performance curve is generated for a model that is 10 times larger than the one shown in Fig. 15. Specifically, the model height and width are now 50 mm, while the fin measures 25 mm in length and 5 mm in height. This corresponds to a total volume 100 times greater than that of the reference problem. For the performance curve, 14 simulations were carried out, with a higher concentration of sampling points around 0.3 H. The results are summarized in Fig. 17. On average, each simulation took 27677 seconds of computation, meaning that a total of 107 hours were needed to construct the performance curve of the enlarged model.

It can be clearly observed that the optimal fin position shifts downward compared to the smaller model, with the best-performing height now located at 0.275 H. The total charging time is 26 times longer than that of the reduced-scale model, allowing sufficient time for convective flow to develop. This can be also noticed in Figs. 18a and 18b, where snapshots of the melting process for the optimal configurations of the small (5×5 mm^2) and large (50×50 mm^2) models are shown, respectively. The figure displays the solid-phase mesh and the velocity streamlines colored by their magnitude. It is evident that the larger model exhibits strong natural convection even at the early stages of melting, whereas the smaller model remains dominated by conduction, resulting in a symmetric melting front with respect to the copper fin.

This example highlights the complexity involved in the design of TES–PCM systems, where simple geometric scaling can completely alter system performance. Similar effects are expected when varying, for instance, the fin geometry, orientation with respect to gravity, or thermophysical properties of the PCM.

4.4 Limitations and applicability

The PFEM framework equipped with the proposed adaptive remeshing strategy is particularly well suited for TES–PCM problems characterized by strong thermal gradients, thin mushy zones, and significant natural convection, where localized mesh refinement is essential to ensure numerical accuracy. In such cases, the ability of PFEM to dynamically adapt the spatial discretization

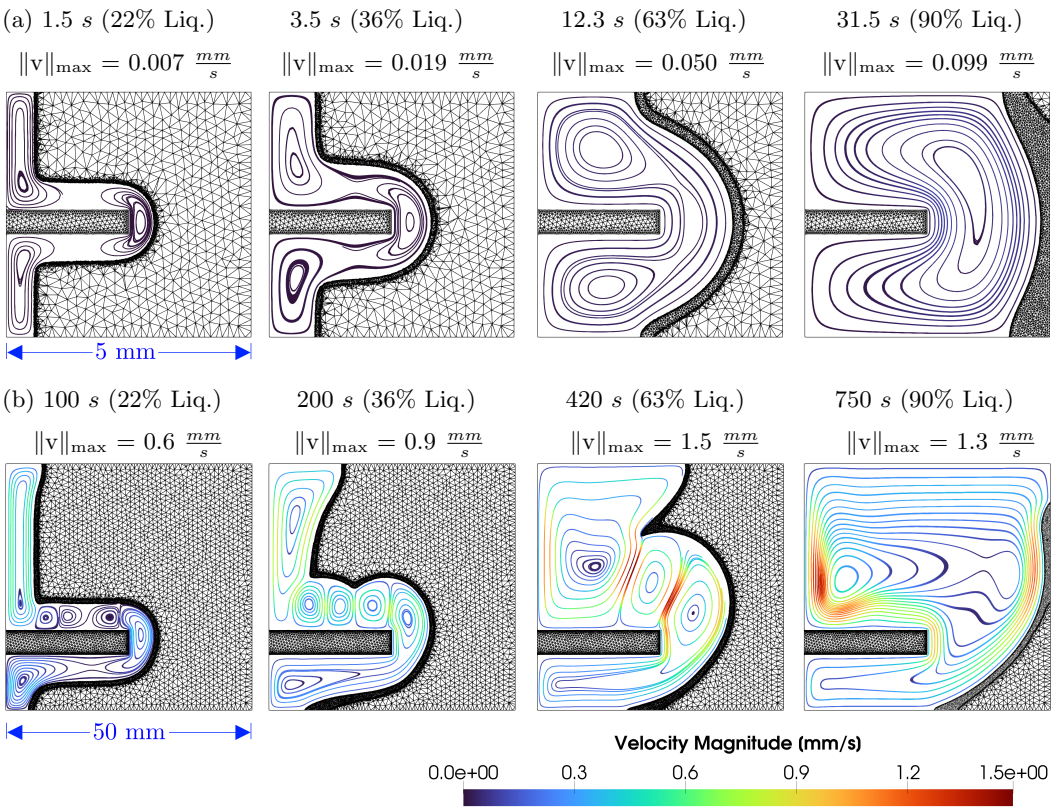

Figure 18: Results of the thermal energy charging process simulation of (a) the small-scale model (5×5 mm^2) proposed by Xu et al. (Xu et al., 2021), and (b) the enlarged model (50×50 mm^2) proposed in this work.

provides a clear advantage over fixed-mesh approaches.

From a computational standpoint, the frequent remeshing inherent to PFEM may limit parallel efficiency compared to classical Eulerian solvers operating on fixed grids, especially in large-scale simulations. While recent developments based on GPU implementations show promising perspectives, the present CPU-based framework remains primarily oriented toward moderate problem sizes and high-fidelity simulations rather than large parametric studies.

Regarding applicability, the proposed approach is not restricted to a specific PCM type and can be applied to materials with different melting temperature ranges, latent heats, and thermal conductivities, provided that a mushy-zone formulation is appropriate. However, the numerical parameters, such as Carman–Kozeny coefficients, mesh adaptation thresholds, and time-step size, must be selected according to the physical properties and operating conditions of each problem.

5 Conclusion

Thermal energy storage based on phase change materials (TES–PCM) has proven to be a promising approach to address the growing energy challenges faced by humanity. Unfortunately, the performance of TES-PCM systems strongly depends on multiple operational and design parameters, making it difficult to fully exploit their potential. In this context, numerical simulation tools are valuable. A review of the literature reveals a clear tendency toward the use of classical simulation methods based on the finite element and finite volume formulations, mainly relying on commercial software that solves the governing equations on a fixed computational mesh.

To the best of our knowledge, our work contributes two main novelties. First, we employ the Particle Finite Element Method (PFEM) for the simulation of TES-PCM systems, which allows for an easy adaptation of the computational mesh during simulation. Second, we propose a new mesh adaptation strategy for PFEM aimed at optimizing the spatial discretization within the mushy zone.

The PFEM method was validated using experimental data from the literature involving lauric acid as PCM. Both experiments, with and without a fin, were successfully reproduced. In addition, the proposed mesh adaptation strategy was validated using the classical melting benchmark of a gallium block. In this case, a 25% reduction in total computation time was achieved with our

contribution compared to the classical distance-based approach. Finally, our PFEM implementation for TES–PCM was verified through a fin-placement optimization problem, yielding results consistent with those reported in the literature.

Although the computational gain is demonstrated for a representative configuration, the proposed mesh adaptation strategy is expected to provide increasing benefits for larger domains and more complex TES–PCM geometries. This is because the mushy zone generally occupies a limited fraction of the computational domain, while regions away from phase change can be discretized more coarsely without affecting solution accuracy. As the size of the system or the geometric complexity increases, the relative reduction in the number of elements becomes more significant. Moreover, since the refinement criterion is driven by local thermal gradients rather than by specific geometric features, the approach is readily applicable to a broad range of TES–PCM configurations and operating conditions. It is also acknowledged that the experimental validation is conducted on relatively simple geometries. Nevertheless, the observed trends are primarily governed by local thermal gradients and mushy-zone dynamics, which are common features across a wide range of TES–PCM applications.

The results obtained in this study suggest that the proposed spatial discretization can be further improved. For instance, our current approach focuses solely on the mushy zone, while the external region is still defined by the classical distance-based adaptation strategy. Clearly, the thermal gradient criterion could be extended beyond the mushy zone and even combined with velocity-gradient-based criteria. Moreover, a 3D extension of the method is entirely feasible. However, our PFEM implementation should be further optimized to reduce computational cost. These developments will be the subject of future research.

Acknowledgments
E. Fernández and M. Lacroix acknowledge the research project TiNTHyN, as part of the Win4Excellence program - convention 2310142, Walloon Region of Belgium.

Disclosure statement
No potential conflict of interest is reported by the authors, and unless otherwise stated, figures and tables are authors' own work.

References

Agrawal, S., Sutheesh, P., Kirankumar, L., and Rohinikumar, B. (2025). Numerical investigations on thermal performance of latent heat thermal energy storage system with novel corrugated annular fins in PCM. *Journal of Energy Storage*, 125:116902.

Akhmetov, B., Navarro, M., Seitov, A., Kaltayev, A., Bakenov, Z., and Ding, Y. (2019). Numerical study of integrated latent heat thermal energy storage devices using nanoparticle-enhanced phase change materials. *Solar Energy*, 194:724–741.

Bobach, B.-J., Boman, R., Celentano, D., Terrapon, V. E., and Ponthot, J.-P. (2021). Simulation of the Marangoni effect and phase change using the particle finite element method. *Applied Sciences*, 11(24):11893.

Bouckaert, S., Pales, A. F., McGlade, C., Remme, U., Wanner, B., Varro, L., D'Ambrosio, D., and Spencer, T. (2021). Net zero by 2050: A roadmap for the global energy sector.

Cabeza, L. F. (2021). Advances in thermal energy storage systems: Methods and applications. In *Advances in thermal energy storage systems*, pages 37–54. Elsevier.

Carman, P. C. (1997). Fluid flow through granular beds. *Chemical engineering research and design*, 75:S32–S48.

Cerquaglia, M. L. (2019). Development of a fully-partitioned PFEM-FEM approach for fluid-structure interaction problems characterized by free surfaces, large solid deformations, and strong added-mass effects. *PhD thesis, University of Liège, Liège, Belgium.*

Çolak, E., Öztop, H. F., and Ekici, Ö. (2022). Analysis of the gallium melting problem with different heating configurations. *Journal of Energy Storage*, 50:104651.

Cremonesi, M., Franci, A., Idelsohn, S., and Oñate, E. (2020). A state of the art review of the particle finite element method (PFEM). *Archives of Computational Methods in Engineering*, 27:1709–1735.

Edelsbrunner, H. and Mücke, E. P. (1994). Three-dimensional alpha shapes. *ACM Transactions On Graphics (TOG)*, 13(1):43–72.

Falla, R., Bobach, B.-J., Boman, R., Ponthot, J.-P., and Terrapon, V. E. (2023). Mesh adaption for two-dimensional bounded and free-surface flows with the particle finite element method. *Computational Particle Mechanics*, 10(5):1049–1076.

Fernández, E., Février, S., Lacroix, M., Boman, R., Papeleux, L., and Ponthot, J.-P. (2023a). A particle finite element method based on Level–Set functions. *Journal of Computational Physics*, 487:112187.

Fernández, E., Février, S., Lacroix, M., Boman, R., and Ponthot, J.-P. (2023b). Generalized-α scheme in the PFEM for velocity-pressure and displacement-pressure formulations of the incompressible Navier–Stokes equations. *International Journal for Numerical Methods in Engineering*, 124(1):40–79.

Fernández, E., Lacroix, M., Février, S., Zhang, T., Papeleux, L., Bobach, B.-J., Boman, R., Ryelandt, S., Simar, A., and Ponthot, J.-P. (2024). Modelling melt pool dynamics in aluminium-to-steel welds performed by friction melt bonding: a challenge addressed with the particle finite element method. *Computational Particle Mechanics*, pages 1–17.

Février, S. (2020). Travail de fin d'etudes: Development of a compressible flow solver for PFEM fluid simulations. *University of Liège, Liège, Belgium*.

Février, S., Fernández, E., Lacroix, M., Boman, R., and Ponthot, J.-P. (2025). Simulation of melt pool dynamics including vaporization using the particle finite element method. *Computational Mechanics*, 75(6):1787–1815.

Fritts, M. and Boris, J. (1979). The lagrangian solution of transient problems in hydrodynamics using a triangular mesh. *Journal of Computational Physics*, 31(2):173–215.

Garoosi, F., Kantzas, A., and Irani, M. (2025). Numerical analysis of thermal performance in Phase Change Material (PCM) melting within rectangular and square enclosures: Impact of design parameters. *Energy*, page 136185.

Gau, C. and Viskanta, R. (1986). Melting and solidification of a pure metal on a vertical wall.

Idelsohn, S. R., Nigro, N. M., Gimenez, J. M., Rossi, R., and Marti, J. M. (2013). A fast and accurate method to solve the incompressible Navier-Stokes equations. *Engineering Computations*, 30(2):197–222.

Idelsohn, S. R., Oñate, E., and Pin, F. D. (2004). The particle finite element method: a powerful tool to solve incompressible flows with free-surfaces and breaking waves. *International journal for numerical methods in engineering*, 61(7):964–989.

Ismail, M., Dincer, I., and Bicer, Y. (2024). Modeling and simulation of nano-enriched latent heat thermal storage system for concentrated solar energy. *Journal of Energy Storage*, 78:110071.

Joshi, V. and Rathod, M. K. (2020). Experimental and numerical assessments of thermal transport in fins and metal foam infused latent heat thermal energy storage systems: A comparative evaluation. *Applied Thermal Engineering*, 178:115518.

Kalapala, L. and Devanuri, J. K. (2021). Effect of orientation on thermal performance of a latent heat storage system equipped with annular fins–an experimental and numerical investigation. *Applied Thermal Engineering*, 183:116244.

Kamkari, B. and Shokouhmand, H. (2014). Experimental investigation of phase change material melting in rectangular enclosures with horizontal partial fins. *International Journal of Heat and Mass Transfer*, 78:839–851.

Kang, Z., Tan, R., Yao, Q., Zhang, J., Zhang, S., and Wei, Y. (2025). Numerical simulation of energy storage radiant floor heating systems with phase change materials having different thermophysical properties. *Construction and Building Materials*, 463:140010.

Kiros, A. K., Zeru, B. A., Desisa, D. G., and Tewolde, D. G. (2025). Fin geometry optimization for enhanced PCM solidification in solar cooking thermal storage system: Numerical simulation and experimental validation. *International Journal of Thermofluids*, page 101243.

Kozeny, J. (1927). Ueber kapillare Leitung des Wassers im Boden. *Sitzungsberichte der Akademie der Wissenschaften in Wien*, 136:271.

Kumar, R. and Verma, P. (2020). An experimental and numerical study on effect of longitudinal finned tube eccentric configuration on melting behaviour of lauric acid in a horizontal tube-in-shell storage unit. *Journal of Energy Storage*, 30:101396.

Lacroix, M. (2025). Robust PFEM-FEM partitioned coupling framework for the simulation of solids under complex flow-induced loads.

Lacroix, M., Fernández, E., Février, S., Papeleux, L., Boman, R., and Ponthot, J.-P. (2026). An efficient level set-based mesh adaptation for the particle finite element method. *Computer Methods in Applied Mechanics and Engineering*, 450:118644.

Lacroix, M., Février, S., Fernández, E., Papeleux, L., Boman, R., and Ponthot, J.-P. (2024). A comparative study of interpolation algorithms on non-matching meshes for PFEM-FEM fluid-structure interactions. *Computers & Mathematics with Applications*, 155:51–65.

Liu, W., Mokhtari, M., Hussein, M. A., Kumar, A., Albayati, T. M., Bains, P. S., Abdul-Redha, H. K., Salahshour, S., and Hekmatifar, M. (2024). Investigation of the arrangement of aluminum fins on the thermal behavior of lauric acid as a phase change material in a two-pipe heat exchanger by CFD simulation. *Case Studies in Thermal Engineering*, 64:105469.

Liu, X., Huang, Y., Zhang, X., Zhang, C., and Zhou, B. (2020). Investigation on charging enhancement of a latent thermal energy storage device with uneven tree-like fins. *Applied Thermal Engineering*, 179:115749.

Meng, E., Xia, T., Zhao, J., Song, Y., Li, J., and Zhao, H. (2025). Numerical study on thermal environment of plastic greenhouse with high absorption latent heat storage plate (LHSP). *Applied Thermal Engineering*, 278:127376.

Nandi, A. and Biswas, N. (2025). Melting dynamics and energy efficiency of nano-enhanced phase change material (NePCM) with graphene, Al2O3, and CuO for superior thermal energy storage (TES). *Journal of Energy Storage*, 109:115076.

Pourakabar, A. and Darzi, A. A. R. (2019). Enhancement of phase change rate of PCM in cylindrical thermal energy storage. *Applied Thermal Engineering*, 150:132–142.

Rodriguez, J., Carbonell, J. M., Cante, J., and Oliver, J. (2016). The particle finite element method (PFEM) in thermo-mechanical problems. *International journal for numerical methods in engineering*, 107(9):733–785.

Rodríguez, J. M., Carbonell, J. M., Cante, J., and Oliver, J. (2017). Continuous chip formation in metal cutting processes using the particle finite element method (PFEM). *International Journal of Solids and Structures*, 120:81–102.

Rozenfeld, A., Kozak, Y., Rozenfeld, T., and Ziskind, G. (2017). Experimental demonstration, modeling and analysis of a novel latent-heat thermal energy storage unit with a helical fin. *International Journal of Heat and Mass Transfer*, 110:692–709.

Sadaka, G., Rakotondrandisa, A., Tournier, P.-H., Luddens, F., Lothodé, C., and Danaila, I. (2020). Parallel finite-element codes for the simulation of two-dimensional and three-dimensional solid–liquid phase-change systems with natural convection. *Computer Physics Communications*, 257:107492.

Safari, V., Abolghasemi, H., and Kamkari, B. (2021). Experimental and numerical investigations of thermal performance enhancement in a latent heat storage heat exchanger using bifurcated and straight fins. *Renewable Energy*, 174:102–121.

Shokouhmand, H. and Kamkari, B. (2013). Experimental investigation on melting heat transfer characteristics of lauric acid in a rectangular thermal storage unit. *Experimental Thermal and Fluid Science*, 50:201–212.

Singh, R. P., Xu, H., Kaushik, S., Rakshit, D., and Romagnoli, A. (2019). Effective utilization of natural convection via novel fin design & influence of enhanced viscosity due to carbon nanoparticles in a solar cooling thermal storage system. *Solar Energy*, 183:105–119.

Tiari, S., Hockins, A., and Mahdavi, M. (2021). Numerical study of a latent heat thermal energy storage system enhanced by varying fin configurations.

Xu, Y., Zheng, Z.-J., Yang, C., and Cai, X. (2021). Intelligent optimization of horizontal fins to improve the melting performance of phase change materials in a square cavity with isothermal vertical wall. *Journal of Energy Storage*, 44:103334.

Zhang, L., Ahmad, S. F., Nutakki, T. U. K., Agrawal, M. K., Ghfar, A. A., Chauhdary, S. T., and Youshanlouei, H. M. (2024). Charging an inclined PCM storage exposed to time-varying solar radiation: Latent heat thermal energy storage. *Journal of Energy Storage*, 90:111911.

Zhang, S., Mancin, S., and Pu, L. (2023). A review and prospective of fin design to improve heat transfer performance of latent thermal energy storage. *Journal of Energy Storage*, 62:106825.

Zhang, W., Zhong, Z.-h., Peng, C., Yuan, W.-h., and Wu, W. (2021). GPU-accelerated smoothed particle finite element method for large deformation analysis in geomechanics. *Computers and Geotechnics*, 129:103856.